Investigating the structure of the windy torus in quasars

S. C. Gallagher,[1][*][†] J. E. Everett,[2] M. M. Abado[1] and S. K. Keating[3]

[1]*Department of Physics & Astronomy, University of Western Ontario, 1151 Richmond St, London, ON N6C 1T7, Canada*
[2]*Center for Interdisciplinary Exploration and Research in Astrophysics (CIERA) and Department of Physics & Astronomy,
Northwestern University, 2145 Sheridan Road, Evanston, IL 60208-3112, USA*
[3]*Department of Astronomy, University of Toronto, 50 St George St, Toronto, ON M5S 3H4, Canada*

ABSTRACT

Thermal mid-infrared emission of quasars requires an obscuring structure that can be modelled as a magneto-hydrodynamic wind in which radiation pressure on dust shapes the outflow. We have taken the dusty-wind models presented by Keating and collaborators that generated quasar mid-infrared spectral energy distributions (SEDs), and explore their properties (such as geometry, opening angle, and ionic column densities) as a function of Eddington ratio and X-ray weakness. In addition, we present new models with a range of magnetic field strengths and column densities of the dust-free shielding gas interior to the dusty wind. We find this family of models – with input parameters tuned to accurately match the observed mid-IR power in quasar SEDs – provides reasonable values of the Type 1 fraction of quasars and the column densities of warm absorber gas, though it does not explain a purely luminosity-dependent covering fraction for either. Furthermore, we provide predictions of the cumulative distribution of $E(B - V)$ values of quasars from extinction by the wind and the shape of the wind as imaged in the mid-infrared. Within the framework of this model, we predict that the strength of the near-infrared bump from hot dust emission will be correlated primarily with L/L_{Edd} rather than luminosity alone, with scatter induced by the distribution of magnetic field strengths. The empirical successes and shortcomings of these models warrant further investigations into the composition and behaviour of dust and the nature of magnetic fields in the vicinity of actively accreting supermassive black holes.

Key words: MHD – galaxies: active – quasars: general – galaxies: Seyfert – infrared: galaxies.

1 INTRODUCTION

Researchers currently studying active galactic nuclei (AGNs) agree on a few key premises. The central engine is powered by a supermassive black hole, and the optical through ultraviolet continuum emission is generated by optically thick material in an accretion disc within the central parsec down to a few gravitational radii. Important specifics such as the thickness of the disc as a function of radius are still being resolved, but the overall picture is consistent; it is hard to avoid disc formation given the persistence of angular momentum. Within the central parsec, ionized gas moving at high velocities covers approximately ~10 per cent of the sky and gives rise to broad (1000s km s^{-1}) resonance and semiforbidden emission lines that characterize Type 1 quasars and Seyfert galaxies. In many luminous quasars, the broad UV emission lines show signatures of winds; the most obvious of these are the P Cygni-type profiles

seen in the high-ionization resonance lines of broad absorption line (BAL) quasars (e.g. Weymann et al. 1991). More subtle are the blueshifts and asymmetries seen in the same lines in other luminous quasars (e.g. Richards et al. 2011). The wind manifested in these lines is likely driven by radiation pressure on ions at UV resonance transitions. For the wind to be launched in the vicinity of the broad-line region (BLR), the quasar continuum must not only have significant power in the UV – the source of the line-driving photons – but not too much power in the X-ray. X-rays will strip atoms such as C and O of their electrons, thus dropping the absorption cross-section dramatically. Overionized gas can therefore only be driven radiatively by Thomson scattering, which is much less efficient than line driving (e.g. Everett & Ballantyne 2004). The elegant picture of Murray et al. (1995) that unifies the broad emission lines seen in all Type 1 quasars with the BAL wind directly observed in only ~20 per cent of optically selected quasars (e.g. Hewett & Foltz 2003) by generating broad emission lines in an equatorial disc wind is compelling, but has not been widely adopted in other models. In such models, broad-line 'clouds' are still invoked as the source of the broad-line emission, though the smoothness of the broad-line profiles and the requirement of some means of pressure

*[*] E-mail: sgalla4@uwo.ca
[†] Visiting Fellow, Yale Center for Astronomy and Astrophysics, Department of Physics, Yale University, New Haven, CT 06520-8120, USA.

confinement to prevent the putative clouds from shredding remain persistently unsolved problems in the cloud picture (e.g. Murray & Chiang 1997; though see Bottorff & Ferland 2000).

An important part of AGN models that is even more uncertain is the so-called torus, a dusty molecular region presumably on the outskirts of the accretion disc. The inner radius of the torus is set by the dust-sublimation radius, beyond which some fraction of the accretion-disc continuum is absorbed by grains and reradiated. Functionally, the torus must account for the ∼30 per cent of the integrated radiant quasar power that comes out in the near-to-mid-infrared. Furthermore, it must obscure the central continuum and BLR in a significant fraction of objects called Type 2 AGN. While a static toroidal structure (whether smooth or clumpy; e.g. Krolik & Begelman 1988; Nenkova, Ivezić & Elitzur 2002; Nenkova et al. 2008) beyond the dust-sublimation radius will serve these purposes, such a cold (100–1500 K) structure with the dust mass implied by the mid-infrared luminosity would quickly become gravitationally unstable and collapse. This problem was addressed by Königl & Kartje (1994) with a magneto-hydrodynamically launched wind, shaped also by radiation pressure on dust. Proposing an alternate dynamical model, Elitzur & Shlosman (2006) use magnetic fields to launch and confine dusty clouds from the plane of the accretion disc. (Lawrence & Elvis (2010) suggest an alternate picture where warped discs, originating from gas in the plane of the host galaxy, account for the large scaleheight needed to obscure the central engine; the gravitational instabilities that can give rise to such asymmetries are further explored by Hopkins et al. 2012.) The dusty-wind picture was expanded by Keating et al. (2012, hereafter K12) by incorporating radiation driving on dust into the magneto-hydrodynamic (MHD) wind models of Everett (2005), and then illuminating the wind with the central continuum to generate a model spectral energy distribution (SED). While the details of the shape of the output continuum still require some refining to match those observed, the overall power and general shape generated by the K12 'fiducial' model is promising. This model uses as inputs the empirical Sloan Digital Sky Survey (SDSS) composite quasar continuum (with the X-ray-to-optical flux ratio, α_{ox}, set to -1.6 as appropriate for the input luminosity; Richards et al. 2006), a black hole mass of $M_{BH} = 10^8$ M$_\odot$, an Eddington ratio of $L/L_{Edd} = 0.1$, and a column density at the base of the wind of $N_{H, 0} = 10^{25}$ cm^{-2}. We further assume a Milky Way interstellar medium (ISM) dust distribution (Draine & Li 2007). In this article, we expand on the results presented in K12 by exploring how key input model properties affect the structure of the wind and extracting other important observables that are generated by the wind model. Finally, we offer some predictions for observations that would further test this picture.

2 THE DUSTY-WIND MODEL

Following Blandford & Payne (1982) and Königl & Kartje (1994), we model the torus as a self-similar dusty wind driven by MHD forces and radiation pressure. The MHD radiative wind code has been described in more detail previously (Everett 2005, K12), and we give only a brief outline here. First, a purely MHD-driven wind solution is calculated given a set of initial conditions input by the user. Next, CLOUDY (version 06.02.09b, as described by Ferland et al. 1998) is called to calculate the radiation field and dust opacity in the wind, allowing for the model to determine the radiative acceleration of the wind due to the central accretion-disc continuum. A new MHD solution is calculated for the wind, now taking into account the radiative acceleration, and the process is iterated until the wind converges to a stable geometry.

Operationally, our assumption of self-similarity means that several important quantities, including magnetic field strength and mass density, scale with spherical radius; this simplifies the calculation of the solution to the MHD equations considerably. Furthermore, it allows for the incorporation of radiation pressure from the disc by simply reducing the effective gravitational potential. Importantly, it allows us to use one streamline as an approximate template for the entire wind, simply scaling appropriately inwards or outwards to find properties of the specific region of the wind under consideration. In addition, these assumptions allow us to comparatively quickly estimate the large-scale properties of these winds. The relevant input parameters and physical properties of the specific models discussed below are presented in Table 1.

2.1 Density distribution

The final, converged MHD radiative wind model therefore provides the mass density of the wind as a function of r, the radial distance from the axis of rotation of the disc, and z, the vertical distance from the plane of the disc. In more detail, the model supplies the density along each streamline as a function of the mass density at the base of the streamline and of polar angle. The density of the wind at any arbitrary point is then relatively straightforward to calculate as a consequence of the self-similarity assumption. Because we know the shape of the wind streamlines, we can use the shape of a single streamline to trace back from an arbitrary point to the disc-launching radius for any wind streamline. From there, given a number density of particles on the disc at the inner launch radius and the fact that density is assumed to be proportional to $r^{-1.5}$ (Blandford & Payne 1982), we calculate the number density at the launch radius of that particular streamline. To convert from number density to mass density, we assign the proton mass to the average particle.

In Fig. 1, we present a 2D colour map of the number density of one quadrant of the dusty wind as a function of r and z for the fiducial model. The inner wind launch radius is set by the dust-sublimation radius. The notable thinness of the wind is a consequence of the model parameters. In general, the outer wind launch radius is given by

$$r_{outer} = r_{in} \left(1 - \frac{N_{H,0}}{2n_{in}r_{in}} \right)^{-2} \tag{1}$$

for user-specified values of the inner launch radius r_{in}, the number density at the inner launch radius n_{in}, and the column density along the base of the wind $N_{H, 0}$.

2.2 Defining the covering fraction

Because the dust is entrained in the wind, $E(B - V)$ (calculated explicitly by CLOUDY) is a smooth function of inclination angle, monotonically increasing towards the plane of the disc where the polar angle $\theta = 90°$. We see this continuous distribution of density as a strength of the dynamical model presented, however, these values offer no obvious inclination angle to choose as the boundary for the wind, and the number density map does not show any obvious feature that would define a 'height' for the torus. The optical depth through the wind is also a smooth function of θ for a wide range of wavelengths, and similarly provides no obvious angle to mark the boundary of the wind. We have therefore chosen the angle at which the dust reaches an optical depth of 5 for light at a wavelength of 6563 Å (the wavelength of Hα emission) to be a conservative definition of the opening angle (i.e. the inclination angle up to which the central engine may be detectable with high signal-to-noise ratio

Table 1. Properties of dusty wind models. All models have $\alpha_{ox} = -1.6$ and $M_{BH} = 10^8$ M$_\odot$ except for model 2 (fid_mbh8p7) with $M_{BH} = 5 \times 10^8$ M$_\odot$.

Model name	κ^a	L/L_{Edd}	$N_{H,shield}^b$ log (cm^{-2})	r_{in}^c (10^{18} cm)	θ_{open}^d (°) $\tau_{H\alpha} = 3$	$\tau_{H\alpha} = 5$	$\dot{m}_{outflow}^e$ (M$_\odot$ yr^{-1})	v_{term}^f (10^3 km s^{-1})
1. fiducial (A)^g	0.03	0.10	18	4.57	62.3	69.4	1.20	2.94
2. fid_mbh8p7 (B)^g	0.03	0.10	18	10.6	62.2	69.3	3.80	5.00
3. fid_edd001 (C)^g	0.03	0.01	18	1.60	60.4	67.3	0.99	1.90
4. sg18_rsublg_k04	0.04	0.10	18	4.57	63.7	70.0	1.21	2.89
5. sg18_rsublg_k06	0.06	0.10	18	4.57	66.9	71.7	1.21	2.89
6. sg18_rsublg_k12	0.12	0.10	18	4.57	74.0	76.5	1.22	2.77
7. sg18_rsubsm_k04_edd05	0.04	0.05	18	3.23	63.0	69.1	1.07	2.81
8. sg18_rsubsm_k06_edd05	0.06	0.05	18	3.23	66.5	71.2	1.07	2.78
9. sg18_rsubsm_k12_edd05	0.12	0.05	18	3.23	73.8	76.4	1.08	2.77
10. sg19_rsub4pt570	0.03	0.10	19	4.57	62.3	69.4	1.20	2.94
11. sg23_rsub4pt480	0.03	0.10	23	4.48	62.3	69.4	1.19	2.95
12. sg24_rsub4pt320	0.03	0.10	24	4.32	62.3	69.4	1.18	2.97
13. sg25_rsub3pt900	0.03	0.10	25	3.90	62.3	69.4	1.13	3.03

Notes. ^{a}Input mass-to-magnetic flux ratio. A smaller value indicates a stronger poloidal B-field.
^{b}Input column density of the shielding (dust-free) gas at the base of the wind.
^{c}The dust-sublimation radius at the base of the wind calculated based on the input parameters. This defines the launching radius of the innermost wind streamline.
^{d}The opening angle of the dusty wind as defined for $\tau = 3$ and 5 at Hα λ6563.
^{e}The mass-outflow rate of the dusty wind.
^{f}The terminal velocity of the dusty wind.
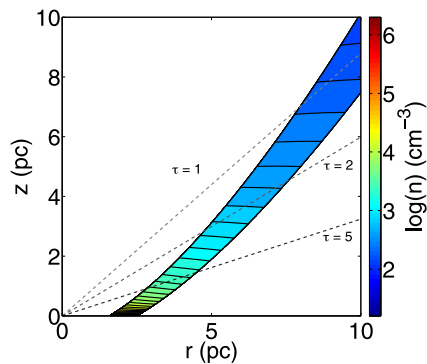^{g}Letters in parentheses refer to the model labels in Fig. 2.

Figure 1. A 2D cross-section of the number density map of the fiducial dusty-wind model with $N_{H,0} = 10^{25}$ cm^{-2}, $M_{BH} = 10^8$ M$_\odot$, and $L/L_{Edd} = 0.1$ (model 1 in Table 1). The colour indicates number density according to the scale bar on the right. The number density drops sharply as a function of height, z, as the wind accelerates. Dashed straight lines indicate the values of the optical depth τ at Hα λ6563, as labelled.

(S/N) spectra to an observer) of the dusty wind. At this value of τ, only 0.7 per cent of the broad Hα emission is transmitted through the wind, and so a quasar viewed from this inclination angle (or closer to the disc) would be classified as an optical narrow-line object. For reference, this value of $\tau_{H\alpha}$ corresponds to $E(B - V) \approx 1.6$ and $A_V \approx 5.5$ (CLOUDY assumes $R_V = 3.4$). For our fiducial model, $\theta_{open} = 69°$; the opening angles for all of the models are listed in Table 1. A value of $\theta_{open} = 69°$ gives a dusty wind covering fraction of $\cos(\theta_{open}) = 35$ per cent. As expected, this is approximately the fraction of the quasar bolometric luminosity that is emitted from 2 to 100 μm in the predicted SEDs from K12. For completeness, we also include the less restrictive opening angle values for $\tau_{H\alpha} = 3$ (corresponding to 5 per cent transmission of the Hα line flux and $A_V \approx 3.3$) which is more relevant for low S/N optical spectra typical of extragalactic survey data.

3 DEPENDENCE OF THE WIND ON INPUT PARAMETERS

3.1 The effect of L/L_{Edd}

Within the context of our model, we can explore variations in windy torus geometries across the AGN population by investigating the effects of changing luminosity, L/L_{Edd}, and M_{BH} on the structure of the wind. Fig. 2 illustrates the shape of the fiducial wind model (labelled as A; model 1 in Table 1) compared to two other models. Model B (model 2 in Table 1) has a black hole mass of 5×10^8 M$_\odot$, five times that of the fiducial model. Because the value of L/L_{Edd} is fixed at 0.1, this model is five times more luminous than the fiducial model. The resulting shape of the wind is nearly identical to that of the fiducial model; the streamlines are slightly more vertical. Model C (model 3 in Table 1) has a black hole mass of 10^8 M$_\odot$ – the same as the fiducial model – but with L/L_{Edd} dialled down to 0.01. The inner launch radius moves in by a factor of $\sqrt{10}$, as expected with an $L^{0.5}$ scaling of r_{in}, and the inner streamlines are more vertical as radiation pressure is relatively less important than at higher Eddington ratios. The slight change in wind structure from altering M_{BH} but keeping L/L_{Edd} constant compared with the larger change from decreasing L/L_{Edd} by a factor of 10 shows that the Eddington ratio is a primary driver given our modelled wind properties.

3.2 The effect of B-field strength

The organized, poloidal magnetic fields in our fiducial MHD-wind model are reasonably strong, with mass-to-magnetic flux ratios of $\kappa = 0.03$, implying considerable magnetic fields strengths of ~0.235 G at the innermost streamline. While an ordered magnetic field is required at the base of the wind to lift material into the line of sight of the accretion-disc continuum, radiation pressure on its own may effectively accelerate material after that point. We explored the effect of dialling down the strength of the magnetic
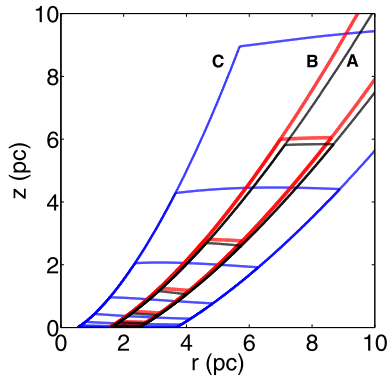
Figure 2. A cross-section of the wind, as in Fig. 1, comparing the profiles of several wind models. Shown here is the fiducial model (black, labelled 'A'; model 1 in Table 1), with $N_{H,0} = 10^{25}$ cm^{-2}, $L/L_{Edd} = 0.1$, and $M_{BH} = 10^8$ M$_\odot$; a similar model with $M_{BH} = 5 \times 10^8$ M$_\odot$ (red, 'B'; model 2 in Table 1); and a third model with the same parameters as the fiducial model except that $L/L_{Edd} = 0.01$ (blue, 'C'; model 3 in Table 1). The dimensions of the model B streamlines have been scaled by $1/\sqrt{5}$ to directly compare the shape of the outflow to the other models. Increasing the black hole mass by a factor of 5 (keeping L/L_{Edd} constant) does not significantly change the shape of the wind, but reducing L/L_{Edd} by a factor of 10 moves the inner launch radius in by a factor of $\sqrt{10}$ (as expected), and causes the inner wind streamlines to be more vertical. This would have the effect of reducing the projected cross-section of the base of the inner wind (which is optically thick to near-IR emission; see fig. 7 in K12) compared to what is seen in the fiducial model. We propose this geometric explanation for the increased prominence of the 3–5 μm bump in luminous quasars.

field. Because $\kappa \propto \frac{1}{B}$, this means increasing κ, and so we ran models with $\kappa = 0.04$, 0.06, and 0.12 for values of $L/L_{Edd} = 0.10$ (models 4–6 in Table 1). Changing B to be up to 4× weaker had a significant effect on the distribution of $E(B - V)$ values over the sky. We found that stronger fields (smaller values of κ) result in higher $E(B - V)$ values over a larger fraction of the sky; the Type 2 boundary for relatively stronger fields occurs at lower inclination angles (69° versus 74° for $\kappa = 0.03$ and 0.12, respectively). These results are a direct consequence of radiation driving dominating when the fields are weaker, thus leading to more radial outflows.

We also ran the different field-strength models for lower L/L_{Edd} values of 0.05 (versus 0.10 for the fiducial model), and found little effect on the cumulative $E(B - V)$ distribution (see Fig. 3; see models 7–9 in Table 1). The lower L/L_{Edd} values also lead to smaller r_{sub} values (and thus r_{in} values for the wind), but the $E(B - V)$ distribution appears to respond most sensitively to increasing κ because radiation pressure consequently becomes more dominant. At mass-to-magnetic flux ratios of $\kappa \sim 1$ the MHD wind will fail, and without an alternate source of vertical lift (e.g. infrared radiation pressure; Dorodnitsyn & Kallman 2012) radiative driving will also not be effective because material from the outer disc will not be exposed to the light from the inner disc.

3.3 The effect of X-ray weakness

Within the context of the dusty-wind model, we are also interested in exploring the effect of the well-known anti-correlation between α_{ox} (the 2 keV to 2500 Å spectral index) and L_{UV} whereby more UV-luminous quasars emit a smaller fraction of their power in the X-rays. For our fiducial model, the value of α_{ox} is -1.6; we have also run models assuming X-ray-loud ($\alpha_{ox} = -1.1$) and X-ray weak
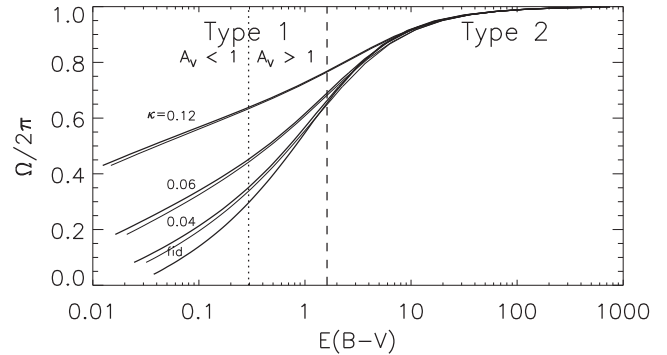

Figure 3. The cumulative covering fraction of the wind ($\Omega/2\pi$) versus extinction, $E(B - V)$; larger $\Omega/2\pi$ values at low extinction show winds that cover less of the sky with significant extinction. The dotted vertical line marks $A_V = 1$, and the dashed vertical line marks the Type 1/Type 2 boundary as defined by $\tau_{H\alpha} = 5$. The mass-to-magnetic flux ratios, κ, for each model are as labelled; with thick (thin) curves representing $L/L_{Edd} = 0.1$ (0.05). The fiducial model curve (marked 'fid') has $\kappa = 0.03$. The curves plotted are for models 1 and 4–9 in Table 1. Decreasing the strength of the magnetic field (increasing κ) increases the importance of radiative driving and makes the wind more radial; consequently, the opening angle of the wind increases and the extinction to Type 1 objects decreases overall.

($\alpha_{ox} = -2.1$) versions of the illuminating SED. Fig. 4 shows the opening angle, θ_{open}, as a function of inner radius, r_{in}. For this large range of α_{ox} values (-2.1 to -1.1 encompasses the extremes of the observed distribution), the effect of X-ray loudness on the opening angle is not large, although two of the X-ray louder models do have slightly larger opening angles ($\theta \sim 75°$) compared to the X-ray quiet ones ($\theta \lesssim 73°$). This result is reasonable, because unlike the ionization parameter of the associated gas, dust driving depends primarily on the integrated *power* in the optical through X-ray, and less on the spectral *shape*.

The models with altered α_{ox} presented in K12 were not particularly realistic, as the X-ray continuum was modelled simply as a flat (in units of power versus frequency) continuum above 0.29 keV whose normalization was set by α_{ox}. In an effort to create a more realistic continuum, we instead include a dust-free layer of shielding gas interior to the dusty wind. The shape of the ionizing continuum impinging on the dusty wind is therefore altered by gas absorption more realistically. To explore the effect of increasing the shielding gas thickness, we ran four additional versions of the fiducial model where only the column density of shielding gas has been altered with values of $\log(N_{H, shield}) = 19$, 23, 24, and 25 cm^{-2} (models 10–13 in Table 1). The fiducial model has $\log(N_{H, shield}) = 18$ cm^{-2}. When we calculate the cumulative distribution of $E(B - V)$ as in Fig. 3, we find that increasing the dust-free shield makes no difference in the shape of that curve, and the opening angles for the dusty wind remain the same as for the fiducial model. Therefore, the shielding gas does not strongly impact the covering fraction of the dusty-wind torus, consistent with the results from our X-ray weak continuum modelling.

4 OBSERVATIONAL CONSEQUENCES OF THE DUSTY-WIND MODEL

The geometric structure, dust distribution, column density, and ionization state of material in the dusty-wind model have direct observational consequences. In K12, we predicted mid-IR SEDs of the wind. Now, we are specifically interested in exploring if the dusty MHD wind can account for the ratio of Type 1 to Type 2 AGNs, the
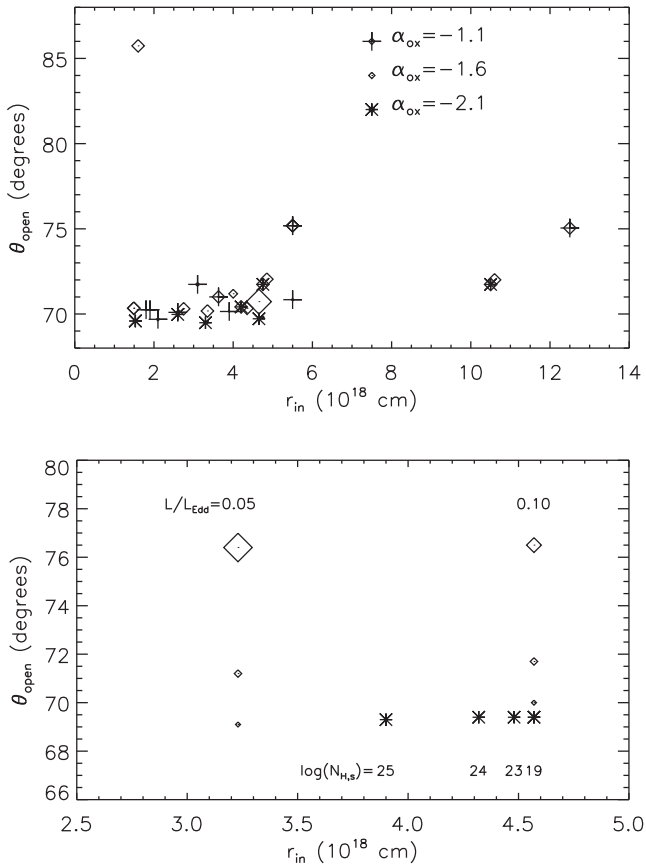
Figure 4. Top: the opening angle, θ_{open} (°), as a function of the wind launch radius, r_{in} (10^{18} cm). All models have base column densities of $N_{H,\,0} = 10^{25}$ cm^{-2}, the value of $N_{H,\,0}$ that generates appropriate near-to-mid-infrared power in the SED (K12). The crosses, diamonds, and asterisks indicate values of α_{ox} as labelled in the legend. The diamonds are scaled to represent their L/L_{Edd} values; the size shown in the legend is $L/L_{Edd} = 0.05$. The models are those presented in K12; the bulk of them give opening angles of 69°–75°. The outlier with $\alpha_{ox} = -1.6$ at $\theta_{open} \approx 86°$ is the model with r_{in} set artificially low to mimic the effect of increasing the dust-sublimation temperature. Bottom: same as panel above for the new models with variable mass-to-flux ratios and variable shielding gas column densities. Diamonds are scaled to represent κ values from 0.03 (smallest, i.e. strongest magnetic field strength) to 0.12 (largest; weakest magnetic field strength). Asterisks show $\kappa = 0.03$ models with a range of shield values (log ($N_{H,\,shield}$) (cm^{-2})) as labelled; all other models have log ($N_{H,\,shield}$) = 18 cm^{-2}. While decreasing the strength of the magnetic field increases θ_{open}, increasing the column density of the shielding gas has little effect on θ_{open}, although the launching radius decreases with increasing $N_{H,\,shield}$.

gross properties and prevalence of warm absorbers, and the near-IR bump from hot dust at ∼1200 K in luminous AGNs.

4.1 Broad- versus narrow-line AGN in the dusty-wind picture

Given the requirement that a successful torus model obscure the accretion-disc continuum and BLR emission, comparing our predicted fraction of Type 1 (optical broad-line) and Type 2 (optical narrow-line) quasars to observations is an important test of the models. In our models, the range of opening angles is relatively tight, and shows little dependence on model input parameters with the exception of the column density at the base of the wind (only models with $N_{H,\,0} = 10^{25}$ cm^{-2} are shown in Fig. 4), and the strength of the magnetic field (see Figs 3 and 4). Specifically for the suite

of models run by K12, typical opening angles using the $\tau_{H\alpha} = 5$ criterion are $\theta_{open} = 69°$–75° (see Fig. 4); this corresponds to dusty-wind covering fractions (Type 2 fractions) of $\frac{\Omega}{2\pi} = \cos(\theta_{open}) = 26$–36 per cent or Type 1 to Type 2 ratios of 1.8 to 2.8. In their survey of low-redshift, emission-line galaxies from the SDSS, Hao et al. (2005) found that Type 1 objects outnumber Type 2 objects by a factor of 2–4 at high luminosities. A similar study by Simpson (2005) found Type 1 fractions of ∼60 per cent (Type 1/Type 2 = 1.5) at the luminous end (in terms of [O III] luminosity). Our numbers are consistent with (though narrower than) the range of 1.5–4 in these population studies.

As demographic studies can be plagued by selection effects, an alternate means of constraining the covering fraction of the dusty 'torus' is to systematically measure the power in the IR-region of Type 1 quasar SEDs. This assumes that the dusty medium acts effectively as an efficient bolometer whose emitted power is simply the fraction of the sky covered by the dusty medium from the point of view of the accretion disc. While radiative transfer modelling shows this is not strictly true (cf. K12), it is a reasonable approximation. Along these lines, the recent analysis by Roseboom et al. (2013) using *WISE* observations of luminous (∼10^{46} erg s^{-1}) Type 1 SDSS quasar determined that the covering fractions could be described by a lognormal distribution with mean of 39^{+23}_{-14} per cent. This corresponds to an intrinsic Type 1/Type 2 ratio ranging from 0.61 to 3.0; the range from our suite of models of 1.8–2.8 is again within (though narrower than) the span of empirical values.

A Type 2 fraction that decreases with increasing luminosity does not follow simply from our model in the parameter range we have explored, as the wind covering fraction is not sensitive to only luminosity, but a combination of L/L_{Edd} and the mass-to-flux ratio of the magnetic field. However, it should be kept in mind that there can be other explanations for a luminosity dependence for obscuration. For example, the host galaxy can also serve as a significant source of obscuration of the BLR (e.g. Rigby et al. 2006; Juneau et al. 2011). If accretion discs are randomly oriented with respect to their host galaxies as observed, the observed Type 2 fractions are inflated with respect to the torus-covering fraction because of line-of-sight obscuration occurring from optically thick dust within the host galaxy (Kinney et al. 2000). Because the size of the BLR scales with luminosity ($\propto L^{0.5}$; Kaspi et al. 2000; Bentz et al. 2009), more luminous BLRs are larger and therefore harder to hide, even before invoking any sort of feedback mechanism that might clear the host galaxy ISM from the vicinity of the quasar. Furthermore, weak broad lines from low-luminosity objects can be 'hidden' by a strong stellar continuum (Moran, Filippenko & Chornock 2002; Martini et al. 2006); detecting these requires high S/N spectra and careful modelling and subtracting of the stellar galaxy emission (e.g. Ho et al. 1997; Hao et al. 2005).

Here, we are defining Type 1/Type 2 as broad line/narrow line with respect to Hα; however, the X-ray community often uses the detection of intrinsic X-ray absorption with $N_H \geq 10^{22}$ cm^{-2} to distinguish obscured versus unobscured quasars. The two criteria overlap, but do not define identical populations, as dust extinction and gas absorption do not always go hand in hand. The N_H value at what we have defined as our Type 1/2 boundary is ∼10^{22} cm^{-2}, and therefore consistent with both the X-ray and optical definitions. In the wind model, this also sets a floor for the amount of intrinsic absorption that would be found in optical Type 2 objects where the dusty wind is obscuring the BLR, consistent with the Seyfert 2 X-ray absorption study of Risaliti, Maiolino & Salvati (1999) and observations of X-ray occultation events by Markowitz, Krumpe & Nikutta (2014).

4.2 Ionic absorption through the wind

4.2.1 Warm absorbers

As seen in Fig. 1, wind density drops quickly as a function of height above the plane of the accretion disc. Because the wind is relatively collimated and narrow radially, this means that the line-of-sight column density also drops rapidly with decreasing inclination angle. The wind at moderate inclination angles is therefore exposed to the high-energy continuum from the accretion disc and becomes highly ionized. Such highly ionized gas along the line of sight to the X-ray continuum is observed in many AGN (∼50 per cent of Seyfert galaxies; e.g. Reynolds 1997); the strongest atomic features of these so-called warm absorbers are the bound–free edges for O VII and O VIII and the helium-like and hydrogen-like inner shell bound–bound transitions of these ions.

Studies of the variability of X-ray absorption features have led to loose constraints on the location of warm absorbers that are largely consistent with the torus location (e.g. within ∼6 pc; Krongold et al. 2005). The specific identification of the warm absorber with a hot phase within the vicinity of a molecular torus has been explored previously. Indeed, this was suggested by Reynolds (1997) when *ASCA* observations revealed the prevalence of warm absorbers in Seyfert galaxies with some preference for those with heavier optical extinction. Subsequently, Krolik & Kriss (2001) explored a multi-temperature thermal-wind origin for the warm absorber gas: they postulated that warm absorbers were evaporated off of the inner surface of the dusty torus.

More recently, Dorodnitsyn & Kallman (2012) presented a radiation-hydrodynamic model that incorporated infrared radiation pressure on dust to drive a slow wind (10–200 km s^{-1}) off of the accretion disc beyond the dust-sublimation radius. The inner (from the point of view of the accretion disc) layer of this slow, cold wind is illuminated by a bright X-ray continuum to form a hot, fast (400–800 km s^{-1}) wind. In the parameter space they considered, UV radiation pressure on dust grains was not included, and the X-ray luminosity needed to power the wind was extremely high, up to $L_X = 0.3 L_{Edd}$, much larger than seen in luminous quasars (where $L_X \sim 0.01 L_{Edd}$ is more typical). The opening angle for the Thomson-thick part of the torus was 72°–75°, which is considerably smaller than our values (close to 90°).

With high S/N X-ray gratings spectra, O VII and O VIII lines and edges in absorption can be used to constrain the column densities of the X-ray absorbing oxygen ions. For reference, two high-quality examples of this type of analysis are based on the 900 ks *Chandra* observation of NGC 3783 (Kaspi et al. 2002) and the simultaneous *Hubble Space Telescope*/*Chandra* study of Mrk 279 (Costantini et al. 2007; Arav et al. 2007); both Seyferts are X-ray bright with particularly strong warm absorber features. The best-fitting column densities from these studies range from 1 to 5×10^{17} cm^{-2} (O VII) and 0.3 to 39×10^{17} cm^{-2} (O VIII). The more recent X-ray study of the reddened quasar IRAS 13349+2438 by Lee et al. (2013) found similarly high column densities of 10^{17-18} cm^{-2} for both ions. From the wealth of features in the High Energy Transmission Grating spectrum, the authors favoured a model with an absorber with a continuous distribution of ionization parameters, and suggested that it could be an ionized atmosphere above the putative torus as in the Krolik & Kriss (2001) picture.

The column densities from these detailed case studies of the strongest (and therefore – by selection – not typical) warm absorbers are about an order of magnitude higher than we find in our fiducial model for O VIII, and about a factor of 100 larger that our
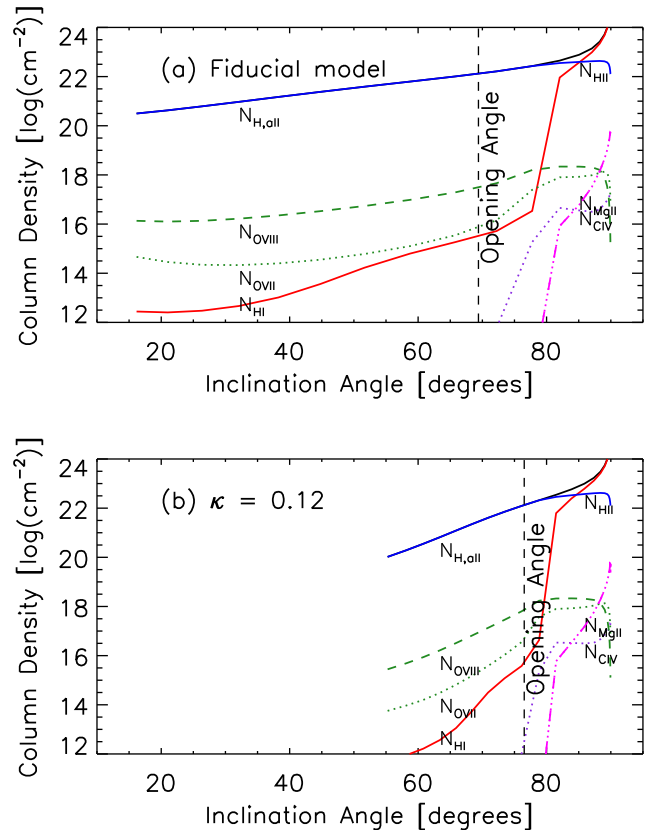
Figure 5. Top (a): column density versus inclination angle of abundant ions characteristic of both high-ionization (e.g. O VII and O VIII) and low-ionization gas (e.g. H I and Mg II) for the fiducial K12 model. Bottom (b): the same plot as above for the lowest *B*-field model with $\kappa = 0.12$. Because of the increased importance of radiative driving, the ionized gas covers a significantly smaller fraction of the sky in this model, and the O VII and O VIII column densities increase more steeply and to larger values than in the fiducial model with $\kappa = 0.03$. In both panels, the column densities of high-ionization gas are largely consistent with constraints from warm absorber studies. The low-ionization species have negligible column densities at inclination angles smaller than the opening angle (marked with a vertical dashed line).

values for O VII (see Fig. 5). Our X-ray weak modification to the fiducial model (with $\alpha_{ox} = -2.1$) however, gives values of O VIII and VII that are both $\sim 10^{17}$ cm^{-2} over a large range of inclination angles. The X-ray loud ($\alpha_{ox} = -1.1$) fiducial model predicts much lower values for the O VIII and O VII column densities because most of the oxygen nuclei are completely stripped of electrons. While the distributions for the fiducial models with the X-ray modifications are all quite flat as a function of inclination angle for $\theta < \theta_{open}$, the $\kappa = 0.12$ model (with the weakest *B*-field), has a much smaller range of angles over which the 'warm absorber' gas would be detected (from $\theta = 55°$–76°), but the hydrogen-like and helium-like oxygen column densities rise steeply as the inclination angle approaches θ_{open}, and near that boundary have values consistent with the empirical values measured from the extreme X-ray spectra cited above (see Fig. 5). Adding a layer of dust-free shielding gas up to $N_{H, shield} = 10^{25}$ cm^{-2} to the fiducial model at most approximately doubles the O VII and O VIII column densities. Given the range of values obtained from the models, we consider the high-ionization gas within the MHD+radiation-driven wind a plausible explanation for more typical (lower column density) X-ray warm absorbers. All

of our models by design have 'dusty warm absorbers'; the dust is collisionally coupled to the gas which is launched and collimated by magnetic fields to large scaleheights where it can be exposed to the X-ray continuum and cover a large fraction of the sky. The model in its present form checks (via CLOUDY) that the gas temperature is consistent with dust survival along the entirety of a streamline to determine the innermost boundary of the wind. None the less, incorporating the data from Figs 3 and 5(a), there is a large range of inclination angles ($\theta = 15°$–$45°$) in the fiducial model with a substantial warm absorber column density of $N_{\rm O\,VIII} \gtrsim 10^{16}$ cm^{-2} without severe reddening ($A_{\rm V} < 1$). The models with weaker B-fields (see Fig. 5 b) generate dusty warm absorbers exclusively.

It is not obvious how one could distinguish observationally between the different proposed scenarios for the warm absorber origin with present data, but future missions such as *Athena+* that will better detect and resolve the velocity structure of X-ray absorption features (including dust signatures; e.g. Lee & Ravel 2005) may shed some light on the relationship of the warm absorbers to a dusty wind. Our models currently provide only integrated column densities of lines of sight through the dusty wind, and so we cannot directly compare absorption profiles as a function of outflow velocity with observed spectra in the UV and X-ray. To provide some reference, the maximum vertical outflow velocities are a few 10^3 km s^{-1} (see Table 1). Warm absorbers typically have multiple velocity components present that can vary independently, and the radiatively driven dusty wind could plausibly account for some of them. However, explaining the details of individual X-ray spectra frequently requires some sort of inhomogeneous structure, and we do not claim that the MHD wind in this iteration of our model is sufficient to account for all of the spectral features. None the less, the presence of highly ionized gas in the dusty outflow occurs naturally within the MHD plus UV/optical and X-ray radiation-pressure-driven model.

4.2.2 Low-ionization gas

If we use Mg II as a tracer of low-ionization gas, it is apparent from Fig. 5 that significant column densities of this ion are not visible in Type 1 objects; the column density of Mg II only rises steeply at inclination angles larger than the opening angle. In this case, the dusty wind alone cannot give rise to the low-ionization gas responsible for broad Mg II absorption lines seen in low-ionization (Lo) BAL quasars. However, in the fiducial model, we have not included a layer of dust-free shielding gas or the UV BAL outflow, as would of course be required for a robust model of BAL quasars. Along the line of sight from the X-ray continuum from the inner accretion disc, BAL quasars have column densities of at least 10^{22} cm^{-2} and low-ionization BAL quasars may be either Compton-thick (e.g. Gallagher et al. 2006) or intrinsically X-ray weak (e.g. Luo et al. 2013) with observed $\alpha_{\rm ox}$ values of $\lesssim -2.0$. (Our addition of MHD-driven shielding gas for some model runs does not include UV-line radiation driving, and so it is not a realistic model for a BAL quasar.)

Relatively rare among optically selected quasars, LoBAL quasars have dust-reddened continua that are intrinsically quite blue (Sprayberry & Foltz 1992; Reichard et al. 2003), and may be evolutionarily young systems (e.g. Farrah et al. 2005; Urrutia et al. 2009). Alternatively, all BAL quasars may have a LoBAL region that is only probed through some fraction of the lines of sight through the wind. This is expected in a radiatively driven wind launched from an accretion disc given the stratified structure of the BLR where

higher ionization gas (probed by C IV) originates at smaller radii than lower ionization gas (probed by Mg II). The similarity of the high-ionization and low-ionization BAL velocity structure (at least at low velocities; Voit, Weymann & Korista 1993) is consistent with both features being found within the same structure launched from a range of radii close to the source of the UV–optical continuum emission and well within the dust-sublimation radius. The dust extinction which is common in LoBAL quasars may however arise from a dust-driven wind as presented in this paper. The concurrence of extinction with LoBALs in a single object therefore would not indicate that there is necessarily dust entrained in the LoBAL outflow; the large inclination angles required to pass through the LoBAL gas are also consistent with larger values of $E(B - V)$ from the dusty wind.

4.3 Hot grains in dusty winds

Within the context of the wind model, we would also like to investigate the empirical observation that the strength of the 3–5 μm bump – the manifestation of a larger contribution to the near-to-mid-infrared SED from hot dust – is seen to increase with increasing quasar luminosity (e.g. Edelson & Malkan 1986; Richards et al. 2006; Gallagher et al. 2007; Krawczyk et al. 2013; Roseboom et al. 2013). In our picture, the inner streamline carries the hottest dust, and it becomes more visible as $L/L_{\rm Edd}$ increases because the relative importance of radiative driving goes up and the wind is pushed closer to the equatorial plane (Gallagher et al. 2007, K12). We predict that this would have the effect of increasing the prominence of the 3–5 μm emission, as the projected cross-section of the surface of the inner streamline from a typical Type 1 orientation angle will increase. The dusty wind becomes optically thick to near-infrared emission at large inclination angles (see fig. 7 in K12). Consequently, within the dusty-wind paradigm, we expect that the claimed correlation of the strength of the 3–5 μm emission with luminosity is in fact a correlation with Eddington ratio. (For luminous quasars, luminosity and $L/L_{\rm Edd}$ are of course correlated given the restricted range of observed black hole masses in flux-limited quasar surveys; e.g. Vestergaard & Osmer 2009.)

A second means of boosting the 3–5 μm emission is to decrease the inner launch radius in the fiducial model by about one-third by increasing the dust-sublimation temperature to approximate the effect of a graphite-driven wind (K12). This decrease in the inner launch radius causes the wind to be notably broader in our model similar to what we saw with the decrease in $L/L_{\rm Edd}$ and as expected from equation (1). However, the *shape* of the streamlines is very close to that of models A and B. Because the bulk of the near-infrared emission is coming from the innermost streamlines, it therefore follows that a smaller $r_{\rm in}$ for a given $L/L_{\rm Edd}$ generates more near-IR emission because of the higher dust temperatures (K12). However, the opening angle for the wind becomes quite large, $\theta_{\rm open} = 86°$ (see Fig. 4). If this is the cause of the luminosity dependence of the 3–5 μm emission, this implies some mechanism for decreasing the dusty wind launching radius as a function of luminosity which is challenging to arrange. We therefore prefer the geometric explanation above.

4.4 Images of the wind

As luminous quasars are typically farther away and therefore fainter and of smaller angular size than nearby Seyferts, they are beyond the reach of the current generation of interferometers. Therefore, we can only compare our simulated model structure to observations

of the nearest Seyfert galaxies, which are by nature considerably less luminous (because of lower M_{BH} masses or lower Eddington ratios or both). A simulated high-resolution image of the wind at 9.5 μm heated by the central continuum is shown in Fig. 6. The hour-glass shape is characteristic of MHD winds, and reminiscent of the outflows seen in young stars. It illustrates clearly that the base of the wind and the inner streamlines dominate the emission at this wavelength; the brightest 9.5 μm emission regions would correspond to the largest extinction values in the optical. Intriguingly, 8–13 μm interferometric observations have led Hönig et al. (2012) to infer a similar structure and characteristic size scale (∼2 pc) for the dust distribution in the Seyfert 2 galaxy NGC 424. The largest compilation of mid-infrared interferometry to date shows that a large fraction of this emission is unresolved, or at scales of <0.1 to <10 pc for a sample of 23 local Seyfert nuclei (Burtscher et al. 2013). Reverberation-mapping using the response of the near-IR continuum to changes in the optical continuum of a several Seyfert galaxies has placed the inner 'torus' radius beyond the BLR and consistent with the expected dust-sublimation radius (Kishimoto et al. 2013). However, more direct comparisons of the dusty-wind models with observations await the light-collecting power and angular resolution (∼0.001 arcsec at 2 μm) expected in the era of 30 m telescopes.

4.5 Constraints on organized magnetic fields

The success of the dusty-wind model that we have presented is predicated on the existence of relatively strong, organized magnetic fields that thread the outer accretion disc of quasars. Certainly, radio-loud AGNs have such fields in the inner disc; radio synchrotron emission from jets requires them. The picture for radio-quiet AGNs is less
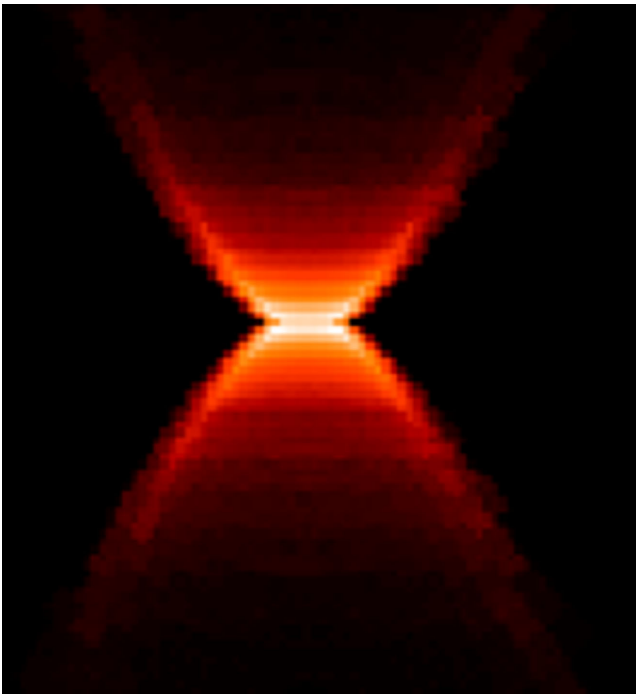

Figure 6. A simulated high-resolution 9.5 μm image of the fiducial model generated by MC3D (Wolf 2003). The hot 'disc'-shaped structure is approximately 2 pc in radius. The bulk of the emission comes from the base of the wind and the inner streamlines heated by the accretion-disc continuum thus giving the MHD wind its characteristic hour-glass shape.

clear. There is some observational evidence for ordered magnetic fields within a few parsecs of the central engine of local AGNs as detected in near-infrared polarimetry. Lopez-Rodriguez et al. (2013) measured polarization of a few per cent in the K_n band for the Type 2 AGN IC 5063. They interpreted the polarization as being due to dichroic absorption of dust grains aligned by magnetic fields in the nuclear region. The polarization properties thus constrain the B-field in the plane of the sky to be 10–130 mG. However, their angular resolution is significantly larger (∼260 pc) than the torus region, and thus the field may be associated with the ISM of the host galaxy near the nucleus, rather than the torus itself. Similarly, from an analysis of Zeeman splitting in OH megamaser emission in ultraluminous infrared galaxies, Robishaw, Quataert & Heiles (2008) estimate magnetic fields strengths of mG are present throughout the ISM in these starbursting galaxies. On smaller scales (a few tenths of a parsec), the lack of detections of circular or linear polarization in measurements of the H_2O molecular masers in Type 2 AGNs gives upper limits of 10–100 mG for the magnetic fields in the masing region (Modjaz et al. 2005; Vlemmings, Bignall & Diamond 2007; McCallum, Ellingsen & Lovell 2007), while our fiducial model has a field strength at r_{in} near the disc surface of ∼0.2G. B-field strengths in our $\kappa = 0.12$ model are a factor of 4 smaller at 50 mG near the disc surface, and therefore still viable given these empirical constraints. Furthermore, the low-luminosity Type 2 AGNs being studied (NGC 4258, NGC 3079, and the Circinus galaxy) may have central regions that are quite different from Type 1 quasars, and so additional empirical constraints on poloidal B-field strengths within the inner parsecs of quasars would be valuable.

5 SUMMARY AND CONCLUSIONS

We explore the properties of the wind models first presented in K12, and extract key parameters including the covering fraction of the optically thick wind, the column densities as a function of opening angle of several ions, and the distribution of extinction values for Type 1 quasars. In addition, we explore the effect of decreasing the strength of the poloidal magnetic field and increasing the column density of the dust-free shielding gas interior to the dusty wind. Altering key input parameters of the model allows us to explore the effects of M_{BH}, L/L_{Edd}, the shape of the ionizing continuum, the mass-to-magnetic flux ratio, and the column density of the shielding gas on the wind. We find the following empirical consequences of this model:

(i) Using our definition of $\tau < 5$ at Hα to define broadline quasars, the dusty-wind model predicts a Type 1 fraction of ∼65 per cent for our fiducial model (Table 1 and Fig. 4). Type 2 quasars in our model have line-of-sight column densities of $N_H \gtrsim 10^{22}$ cm^{-2} (Fig. 5). Both of these values are roughly consistent with observed Type 1 fractions and line-of-sight column densities found in optical and X-ray surveys of luminous AGNs and from mid-IR SED analyses.

(ii) While the presence of a UV line-driven wind as seen in BAL quasars apparently requires a blue UV continuum and weak X-ray emission (either as a result of absorption or intrinsic weakness), the dust-driven wind is much less sensitive to the *shape* of the continuum. Mid-IR continuum emission might therefore be quite similar among classes of quasars with a range of ionizing SED shapes, and consequently a more accurate measure of bolometric luminosity.

(iii) We present predictions for the cumulative distribution of $E(B - V)$ values for quasars (Fig. 3). The normalization of these

curves depends primarily on κ, the mass-to-magnetic flux ratio, with higher values of κ (weaker B-fields) resulting in slightly larger opening angles, and significantly less dust extinction over a wide range of opening angles. This is a consequence of radiation pressure dominating over magnetic driving which results in more radial outflows. The effect of changing κ has a larger effect on the $E(B - V)$ distribution than changing L/L_{Edd} within the range we considered.

(iv) The column density through the wind drops rapidly with height from the disc causing the ionization parameter of the wind to increase dramatically. As a consequence, high-ionization atomic species are present at a large range of inclination angles. The modelled values for the column densities of O VIII through the wind are $\sim 10^{16-18}$ cm^{-2} depending on the properties of the ionizing continuum and the value of κ (Fig. 5). This range is low for the strongest X-ray warm absorbers in the best-studied local Seyfert galaxies, but consistent with more typical warm absorbers. Improved measurements of the profiles of warm absorber features with next generation X-ray observatories may determine if the dusty-wind model presented here remains a viable explanation for X-ray warm absorbers.

(v) The hot dust emission present in the near-IR SEDs of luminous quasars could be associated with the innermost surface of the dusty wind, where grains with higher sublimation temperatures than silicates can survive. We predict that the strength of this emission feature will correlate with L/L_{Edd} as higher L/L_{Edd} flows are more radial, and the cross-section of the inner streamline visible to the observer at typical inclination angles becomes larger. Scatter could be introduced in this correlation by a distribution of magnetic field strengths at given values of L/L_{Edd}.

(vi) MHD+radiation-driven wind models of the AGN 'torus' predict hour-glass shapes for the mid-IR emission which may be routinely detectable in nearby AGN with improvements in near-to-mid-IR interferometry and the next generation of 30 m class telescopes. The shape of the innermost streamline (which generates the bulk of the emission) is most sensitive to the mass-to-magnetic flux ratio, and secondly to L/L_{Edd}.

Getting the dusty-wind model to the point where it can plausibly account for the detailed structure in near-to-mid-infrared quasar SEDs requires additional refinement. In particular, the current single-zone dust structure is not realistic, and the dust composition and grain-size distribution likely varies from that of the Milky Way ISM as assumed in our models. The need for different dust properties for quasar environs is already implied by observations indicating that the shape of the extinction curve to most quasars is more consistent with Small Magellanic Cloud (SMC)-type dust (e.g. Krawczyk et al. 2015).

While clouds are not likely to persist in the dynamic environment around a supermassive black hole (e.g. Schartmann, Krause & Burkert 2011), it is also unlikely that any wind structure is completely smooth. Including inhomogeneities in the wind is therefore an obvious next step, in particular to more realistically predict ionic column densities.

More generally, the viability of the dusty MHD disc wind paradigm requires an investigation into whether relatively strong ($\gtrsim$ 50 mG), large-scale poloidal magnetic fields persist within the central parsecs of quasar host galaxies. Certainly quasars with jets have large-scale magnetic fields; radio synchrotron emission is observed. In the near future, the available sensitivity and spatial resolution of *ALMA* and the Jansky Very Large Array are promising for placing meaningful constraints on the strengths of organized fields within the central few parsecs of radio-quiet AGNs.

REFERENCES

Arav N. et al., 2007, ApJ, 658, 829
Bentz M. C., Peterson B. M., Netzer H., Pogge R. W., Vestergaard M., 2009, ApJ, 697, 160
Blandford R. D., Payne D. G., 1982, MNRAS, 199, 883
Bottorff M. C., Ferland G. J., 2000, MNRAS, 316, 103
Burtscher L. et al., 2013, A&A, 558, A149
Costantini E. et al., 2007, A&A, 461, 121
Dorodnitsyn A., Kallman T., 2012, ApJ, 761, 70
Draine B. T., Li A., 2007, ApJ, 657, 810
Edelson R. A., Malkan M. A., 1986, ApJ, 308, 59
Elitzur M., Shlosman I., 2006, ApJ, 648, L101
Everett J. E., 2005, ApJ, 631, 689
Everett J. E., Ballantyne D. R., 2004, ApJ, 615, L13
Farrah D., Surace J. A., Veilleux S., Sanders D. B., Vacca W. D., 2005, ApJ, 626, 70
Ferland G. J., Korista K. T., Verner D. A., Ferguson J. W., Kingdon J. B., Verner E. M., 1998, PASP, 110, 761
Gallagher S. C., Brandt W. N., Chartas G., Priddey R., Garmire G. P., Sambruna R. M., 2006, ApJ, 644, 709
Gallagher S. C., Richards G. T., Lacy M., Hines D. C., Elitzur M., Storrie-Lombardi L. J., 2007, ApJ, 661, 30
Hao L. et al., 2005, AJ, 129, 1795
Hewett P. C., Foltz C. B., 2003, AJ, 125, 1784
Ho L. C., Filippenko A. V., Sargent W. L. W., Peng C. Y., 1997, ApJS, 112, 391
Hönig S. F., Kishimoto M., Antonucci R., Marconi A., Prieto M. A., Tristram K., Weigelt G., 2012, ApJ, 755, 149
Hopkins P. F., Hayward C. C., Narayanan D., Hernquist L., 2012, MNRAS, 420, 320
Juneau S., Dickinson M., Alexander D. M., Salim S., 2011, ApJ, 736, 104
Kaspi S., Smith P. S., Netzer H., Maoz D., Jannuzi B. T., Giveon U., 2000, ApJ, 533, 631
Kaspi S. et al., 2002, ApJ, 574, 643
Keating S. K., Everett J. E., Gallagher S. C., Deo R. P., 2012, ApJ, 749, 32 (K12)
Kinney A. L., Schmitt H. R., Clarke C. J., Pringle J. E., Ulvestad J. S., Antonucci R. R. J., 2000, ApJ, 537, 152
Kishimoto M. et al., 2013, ApJ, 775, L36
Königl A., Kartje J. F., 1994, ApJ, 434, 446
Krawczyk C. M., Richards G. T., Mehta S. S., Vogeley M. S., Gallagher S. C., Leighly K. M., Ross N. P., Schneider D. P., 2013, ApJS, 206, 4
Krawczyk C. M., Richards G. T., Gallagher S. C., Leighly K. M., Hewett P. C., Ross N. P., Hall P. B., 2015, AJ, 149, 203
Krolik J. H., Begelman M. C., 1988, ApJ, 329, 702
Krolik J. H., Kriss G. A., 2001, ApJ, 561, 684
Krongold Y., Nicastro F., Brickhouse N. S., Elvis M., Mathur S., 2005, ApJ, 622, 842
Lawrence A., Elvis M., 2010, ApJ, 714, 561
Lee J. C., Ravel B., 2005, ApJ, 622, 970
Lee J. C. et al., 2013, MNRAS, 430, 2650
Lopez-Rodriguez E. et al., 2013, MNRAS, 431, 2723
Luo B. et al., 2013, ApJ, 772, 153
McCallum J. N., Ellingsen S. P., Lovell J. E. J., 2007, MNRAS, 376, 549
Markowitz A. G., Krumpe M., Nikutta R., 2014, MNRAS, 439, 1403

Martini P., Kelson D. D., Kim E., Mulchaey J. S., Athey A. A., 2006, ApJ, 644, 116

Modjaz M., Moran J. M., Kondratko P. T., Greenhill L. J., 2005, ApJ, 626, 104

Moran E. C., Filippenko A. V., Chornock R., 2002, ApJ, 579, L71

Murray N., Chiang J., 1997, ApJ, 474, 91

Murray N., Chiang J., Grossman S. A., Voit G. M., 1995, ApJ, 451, 498

Nenkova M., Ivezić Ž., Elitzur M., 2002, ApJ, 570, L9

Nenkova M., Sirocky M. M., Nikutta R., Ivezić Ž., Elitzur M., 2008, ApJ, 685, 160

Reichard T. A. et al., 2003, AJ, 126, 2594

Reynolds C. S., 1997, MNRAS, 286, 513

Richards G. T. et al., 2006, ApJS, 166, 470

Richards G. T. et al., 2011, AJ, 141, 167

Rigby J. R., Rieke G. H., Donley J. L., Alonso-Herrero A., Pérez-González P. G., 2006, ApJ, 645, 115

Risaliti G., Maiolino R., Salvati M., 1999, ApJ, 522, 157

Robishaw T., Quataert E., Heiles C., 2008, ApJ, 680, 981

Roseboom I. G., Lawrence A., Elvis M., Petty S., Shen Y., Hao H., 2013, MNRAS, 429, 1494

Schartmann M., Krause M., Burkert A., 2011, MNRAS, 415, 741

Simpson C., 2005, MNRAS, 360, 565

Sprayberry D., Foltz C. B., 1992, ApJ, 390, 39

Urrutia T., Becker R. H., White R. L., Glikman E., Lacy M., Hodge J., Gregg M. D., 2009, ApJ, 698, 1095

Vestergaard M., Osmer P. S., 2009, ApJ, 699, 800

Vlemmings W. H. T., Bignall H. E., Diamond P. J., 2007, ApJ, 656, 198

Voit G. M., Weymann R. J., Korista K. T., 1993, ApJ, 413, 95

Weymann R. J., Morris S. L., Foltz C. B., Hewett P. C., 1991, ApJ, 373, 23

Wolf S., 2003, Computer Phys. Comm., 150, 99

This paper has been typeset from a TEX/LATEX file prepared by the author.